

Research

Mineralogy and rare earth elements spatial distribution in the carboniferous rocks of the eastern El Galala El Bahariya, Egypt

Randa S. Ramadan¹ · Mohamed M. Abu-zeid¹ · Ashraf R. Baghdady¹ · Ahmed Gad^{1,2} · Yehia H. Dawood¹ · Shaimaa M. El-hadidy¹ 

Received: 27 December 2023 / Accepted: 5 June 2024

Published online: 11 July 2024

© The Author(s) 2024 [OPEN](#)

Abstract

The Carboniferous rocks in the eastern part of El Galala El Bahariya were investigated using integrated field and laboratory techniques to determine their mineralogy, rare earth elements (REEs) distribution, and structural lineament density. The succession is mainly composed of argillaceous and minor arenaceous rocks, exhibiting variations in lithology across the study area. The essential minerals of these rocks are quartz, kaolinite, and illite. The accessory minerals include microcline, gypsum, anhydrite, halite, barite, hematite, pyrite, anatase and gibbsite, in addition to, the radioactive and REEs-bearing minerals such as uranophane, xenotime, monazite, and zircon. These minerals are reported in the rocks of the study area for the first time. The types, forms, habits, and modes of occurrence of the recorded minerals indicate multiple origins: allogenic–authigenic, and primary–secondary. REEs in the rocks exhibit enriched patterns with a negative Eu anomaly, likely due to low plagioclase content or and/or Eu removal by alteration processes. The distribution of REEs is influenced by textural attributes, with finer sediments in the southern part showing higher REEs content, ascribed to the high clay content and presence of gibbsite. The preferential mobility of LREEs is evident, explaining elevated LREEs/HREEs ratios in the rocks. Utilizing remote sensing techniques, lithological units and alteration zones were determined using decorrelation stretch and band ratio methods. The structural features, identified by Laplacian filter and edge enhancement, revealed the presence of NW–SE, N–S, and NE–SW faults that structurally regulate alteration zones and REEs distribution. These alteration zones are associated with clay minerals, REEs concentrations, and high lineament structure density. Spatial distribution maps highlight higher REEs concentrations in the southern part of the study area. These findings were validated using various analytical methods, including mineralogical and geochemical investigations, main component analysis, minimum noise fraction, decorrelation stretch, and spectral reflectance studies. They provide new insights into the REEs potential of the Carboniferous rocks and heighten our understanding of REEs genesis and distribution in the region.

Article Highlight

- Collaborative use of remote sensing, mineralogy, and geochemistry to explore REEs distribution.
- LREEs demonstrate higher mobility than HREEs in surface environments.
- Multiple origins revealed through mineral types, forms, habits, and modes of occurrence.

✉ Shaimaa M. El-hadidy, elhadidy_sh@sci.asu.edu.eg | ¹Geology Department, Faculty of Science, Ain Shams University, Cairo, Egypt. ²College of Science, Geosciences Department, United Arab Emirates University, Al Ain 15551, UAE.



Keywords Carboniferous · El Galala El Bahariya · Siltstones · Rare earth elements · ASTER data processing · Lineament · Remote sensing

1 Introduction

The fine-grained clastic sedimentary rocks such as siltstones and shales are the most potential sedimentary rock types for uranium and rare earth elements (REEs). Also, these rocks are usually enriched in sensitive redox elements such as Cr, V, Mo, Re, U, As, Cd, Ab, Se, Ag, Cu, Ni, Zn, Co, and Pb [1]. The adsorption and distribution of REEs and other precious metals in the near-surface environment are crucial factors in understanding their cycle in the earth's crust. This understanding is important for the exploration of new resources of these elements as well as environmental management [2]. REEs are commonly used to identify sediment source areas, paleoenvironment and paleoclimate [3]. In addition, REEs geochemical data can be used along with other geological parameters to study sedimentary environments and tectonic settings [4], and as fingerprints of water–rock interactions [5]. The adsorption of REEs is mainly related to clay contents, types of clay minerals, pH, cation-exchange capacity (CEC) and the concentrations of aluminum and manganese oxides that have high adsorption capacity [6–8]. On the other hand, organic matter has a fundamental role in the adsorption of REEs since it has a reactive negative charge.

Multisource geological data can be used to get information in mineral exploration and the distribution of elements in the rocks. For instance, remote sensing images record the spectral characteristics of rocks, and geochemical data represent the enrichment or depletion of elements. Laakso et al. [9] provided a review of a limited number of published studies devoted to spectral properties of REE in the LWIR range emphasizing that it has not yet been satisfactorily solved whether the LWIR range contains useful information about their identification. Booyesen et al. [10] demonstrated for the first time the feasibility to identify REE in carbonatite outcrops in arid and subarctic environments using hyperspectral data acquired by lightweight UAV. Although REEs cannot be detected by satellite multispectral instruments, their distribution can be identified using a new Aster band ratio scheme [11].

As the authors are aware, the present study is the first contribution to the mineralogy and REEs geochemistry of the Carboniferous rocks in eastern El Galala El Bahariya. In this study, the results of integrated field and laboratory investigations (involving remote sensing) were used to obtain a more accurate picture of the distribution of REEs in the Carboniferous rocks of the study area.

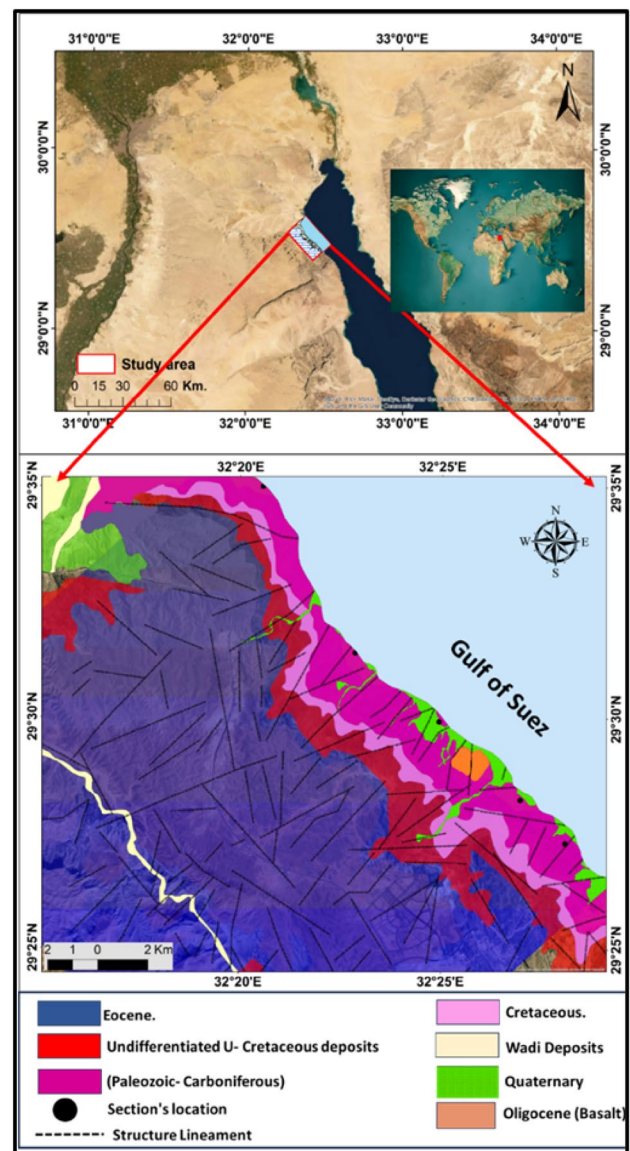
2 Geologic setting

El Galala El Bahariya Plateau is located in the western side of the Gulf of Suez between Ain Sokhna and Zafraana cities. It occupies an area of about 19,000 acres. The Plateau extends for about 80 km from west to east with the highest elevation of 1260 m above sea level. EL Galala El Baharyia Plateau is bordered by Wadi Ghewibba and Wadi Araba at the north and south; respectively. It is dissected by some wadis and the main tributaries from west to east are W. El Qena, W. Abu Diaba, W. El-Abyad, W. Naooz, W. Umm Russeies and W. Harooz. These tributaries compose a part of Wadi Ghewibba catchment area. Stratigraphically, the area is covered by several lithological units ranging in age from Upper Paleozoic (Permo-Carboniferous) and Permo-Triassic to Lower Mesozoic clastics and carbonates (Triassic to Early Cretaceous). This is overlain by marine suites of Cenomanian to Middle Eocene age [12–14]. Structurally, it falls in two overlapping structural provinces, namely the Syrian arc folds and fault system and the Gulf of Suez rift. The exposed Carboniferous layers in El Galala El Bahariya Plateau and Wadi Araba area were first discovered by [12]. The stratigraphy of these layers was later carried out by [13]. Abdallah and El-Adindani [14] were the first to subdivide the Carboniferous succession in Wadi Araba and Abu El-Darag areas into three formations; namely: Rod El-Hamal, Abu Darag and Aheimer. Rod El-Hamal Formation coevals with the Ataqa Formation of the Carboniferous succession of the eastern side of the Gulf of Suez [13, 15]. Rod El-Hamal Formation is overlain by the Permian–Triassic succession (Qiseib Formation). The study area is located at the eastern scarp of El Galala El Bahariya. It lies between latitudes 29° 24' and 29° 32' N and longitudes 32° 18' and 32° 22' E. It contains a thick Carboniferous succession that is dominated by argillaceous rocks, the majority of which were previously described as shales.

The Syrian Arc highs in the Sinai Peninsula (including the El-Galala mountain range) strike WSW–ENE [16]. Abou El Saoud [17] emphasized that the area in the Cairo-Suez District is structurally controlled by three tectonic events. These are the Syrian Arc System with a NE–SW trend, the Gulf of Suez rift which NW–SE dominates to NNW–SSE

normal faults, and the Dead Sea fault which represents the youngest tectonic event and has a left-lateral strike-slip movement. According to the tectonic position of the El Galala Plateau, three major depositional units developed on a rimmed shelf may be distinguished. These are the northern El Galala High, the Wadi Araba transitional slope zone and the southern El Galala sub-basin [16, 18]. Basaltic dyke is found cutting the siltstones in the study area. The Oligo-Miocene volcanic activity is represented mainly by basaltic dykes trending NNW–SSE parallel to the long axis of the Red Sea and was contemporaneous with the initial phase of Sinai uplifting and rifting of the Red Sea and Gulf of Suez [19]. The history of deformation along the Red Sea margin has had a significant impact on the evolution of this area. The image properties (tone and texture), lithological boundaries (rock units), and geomorphological aspects (drainage patterns) were used to extract lineaments and visual interpretation criteria. The structural lineaments in the study area have four primary fault trends: NW, NE, N–S, and ENE. These trends support one another and demonstrate that the structural characteristics trend follows the NW–SE, NE–SW, and ENE–WSW directions. The lineament map also shows other minor trends in the NNW–SSE and NNE–SSW axes (Fig. 1).

Fig. 1 Surface lineament overlaid on rock units map of El Galala El Bahariya (modified after [20])



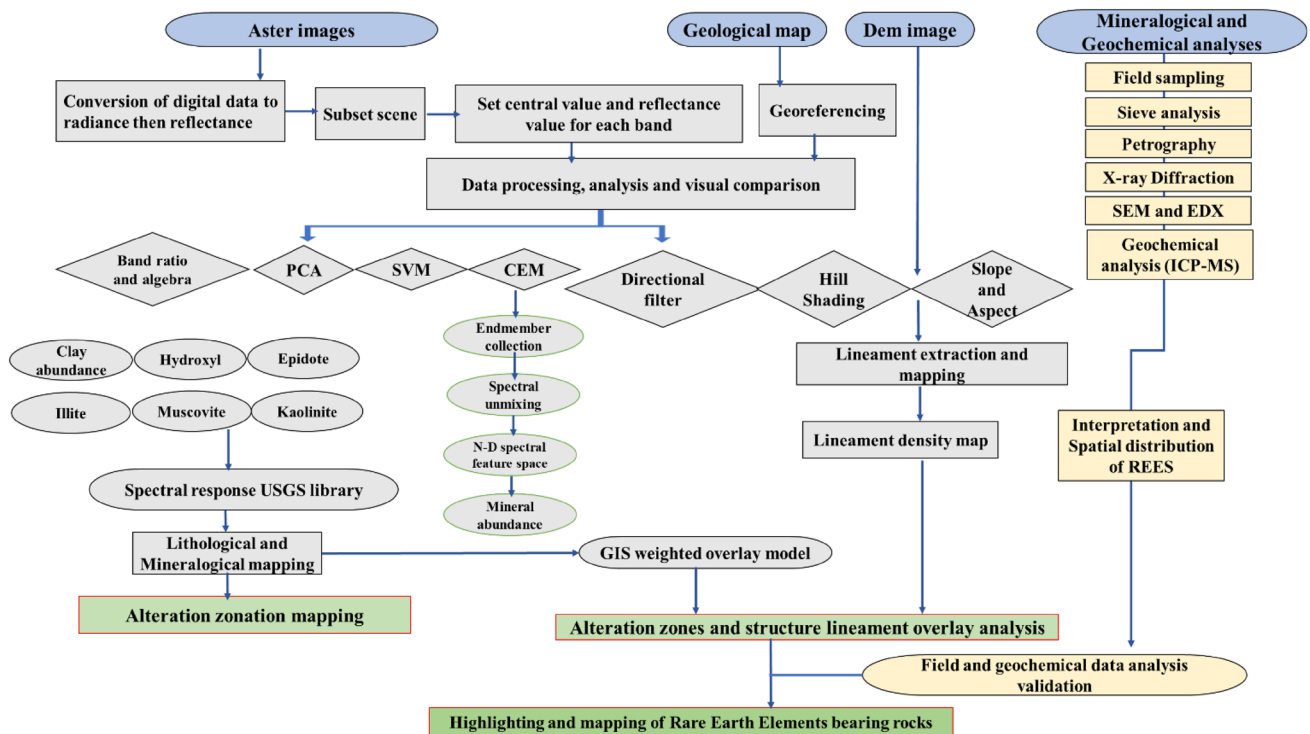


Fig. 2 Flow chart of the used techniques and methodology

Table 1 The main band math applied to discriminate the different minerals associated with alteration and REEs

Mineral index	Band math	References
Sericite-illite-	$[(B5 + B7)/B6]$	[23]
Kaolinite	$(B7 - B5)$	[24]
OH group	$((B7/B6) * (B4/B6))$	[23]
Ferrous silicate	$(B5/B4)$	Derived from specific sensor formula
Clay index	$(B1 - B7)/(B6 - B6)$	[25]
Argillic-non argillic	$(B5/B7)$	Derived from specific sensor formula
Quartz Rich	$(B14/B12)$	[25]
Epidote-chlorite	$(B6 + B9)/(B7 + B8)$	[23]
Amphibole	$(B6)/(B8)$	[24]
Muscovite	$(B7)/(B6)$	[24]
CO ₃ -epidote	$(B7 + B9)/B8$	[25]
Ferric-Ferrous	$B3 - B1$	[23]
Alteration	$B4/B5$	[26]

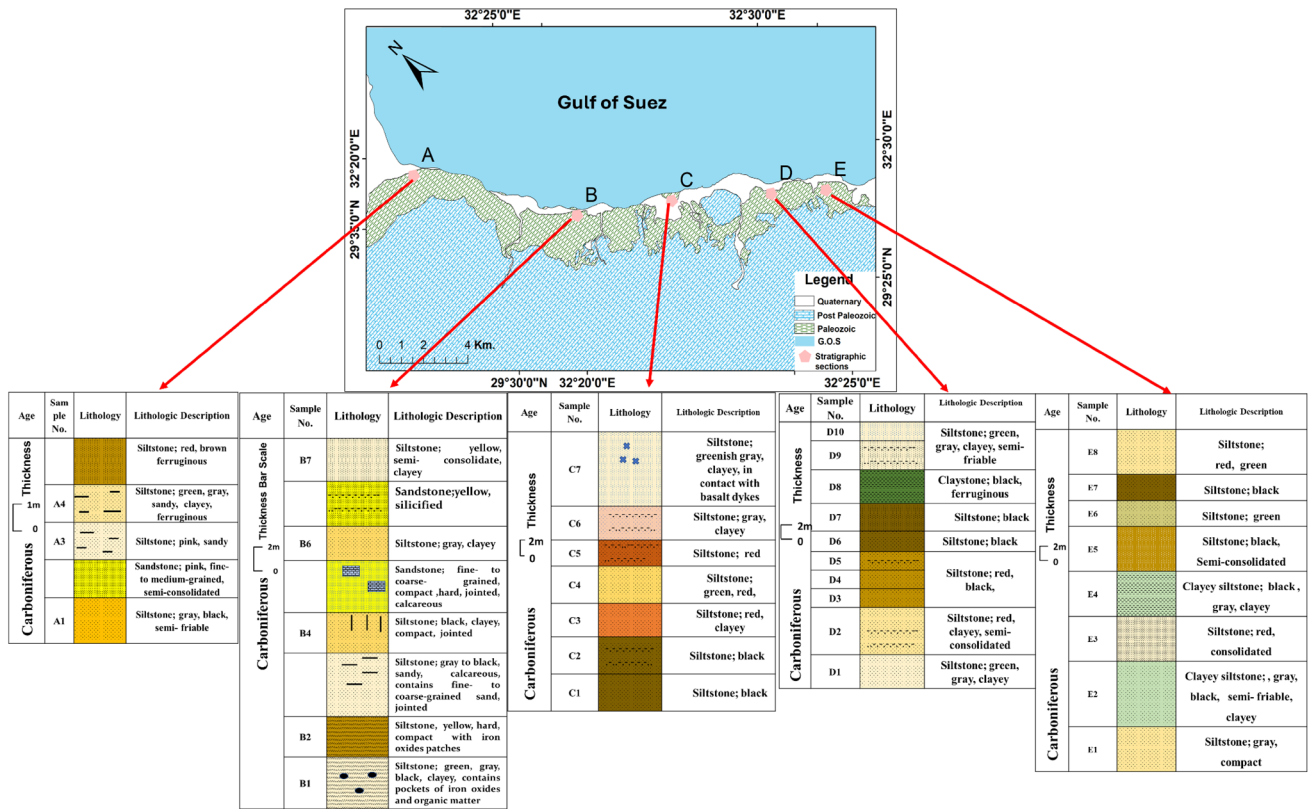


Fig. 3 Lithostratigraphic columns of the studied sections (A, B, C, D and E)

3 Materials and methods

3.1 Remote sensing

3.1.1 Satellite data acquisition, preprocessing and image restoration

Digital image processing techniques, Thermal Emissivity and Reflection Radiometer Sensor (ASTER level 1B scene, May 20, 2015) were used to map alteration zones' spatial and spectral extent. These data were downloaded from <https://LPDAAC.gov> with WGS 84—Zone 36 N projection. Images were edited for atmospheric effects using ENVI software. SRTM (DEM) of 30 m resolution was obtained from the geospatial data cloud <http://earthexplorer.usgs.gov>.

The satellite images corrections for defects, such as atmospheric noise, involve thermal correction of Aster-TIR emittance bands and rapid line of sight part analysis of spectral hypercubes (FLAASH). These techniques convert component radiance at the sensor element data coefficient of reflection and extract spectral reflectance by ENVI 5.3 software. This process is crucial for mineral resource study including image restoration, enhancement, and information extraction.

The digital ASTER data were preprocessed using mosaic, atmospheric correction, and layer stack VNIR-SWIR bands techniques. These bands are crucial for geology, covering key absorption features of minerals. The ASTER L1B data were radiometrically calibrated, spatially co-registered and derived from the radiance at the sensor product. The reflectance and emissivity of the utilized materials and information were derived from remote sensing data for mineral resource analysis.

Fig. 4 Spatial distribution of the various textural rock types in the study area

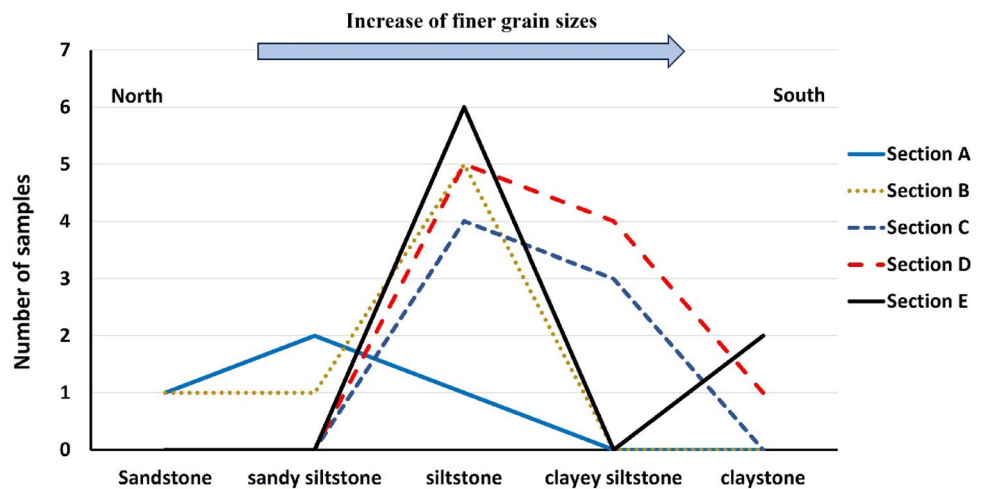


Table 2 Summary of the lithological and mineralogical characteristics of the studied Carboniferous rocks

Rock type	Number of samples	Essential minerals			Accessory minerals	
		Nonclay	Clay minerals	No. of samples	Non-radioactive	Radioactive and REEs-bearing
Siltstone	21	Quartz	Kaolinite	28	Microcline	Uranophane
Clayey siltstone	9		Illite	19	Gypsum	Xenotime
Sandy siltstone	3		Chlorite-illite	6	Anhydrite	Monazite
Sandstone	2				Halite	Zircon
Claystone	1				Barite	
					Hematite	
					Pyrite	
					Anatase	
					Gibbsite	

3.1.2 Satellite data processing

The material’s reflectance, emissivity, and information were acquired from remote sensing data for mineral investigations. To choose the principal bands, the spectral properties of minerals in the host rock were studied. Figure 2 illustrates the used methodology in the current study.

The images with highly correlated bands were enhanced to reduce redundancy by applying decorrelation stretch (DS). Principal component analysis (PCA) was used to discriminate rock contacts. Based on field observations and geochemical analysis, the REEs spatial distributions were determined using Ordinary kriging (OK) in ArcGIS software (version 10.8). The band ratios are not considered indicators for the existence and quantity of a mineral with absolute certainty. So, field validation and establishing appropriate thresholds are crucial [21]. The spectral characteristics of minerals in the host rock were examined to choose influential bands. Various band ratios and false-color composites were produced to determine which band ratios and false-color composites are best for identifying iron mineralization, alunite, kaolinite, chlorite-epidote assemblage, and argillic alteration.

The clay mineral ratios were used to emphasize the clay minerals abundance in the rocks. Table 1 summarizes all band algebra used in the alteration mapping. Density slicing was used to convert the continuous grey tone into a set of density slices. A comprehensive assessment of the structures in the area was performed using SRTM topographic data (DEM) [22]. Remote sensing methods such as enhancement, linear, edge filtering, visual interpretation, aspect, and hill shading were used in ArcGIS to generate thematic maps depicting the lineament pattern in various directions (45, 60, 90, 180, and 270 azimuths). Density values were calculated in ArcGIS using the Kernel Density tool, spatial filtering with a 5 * 5 kernel size.

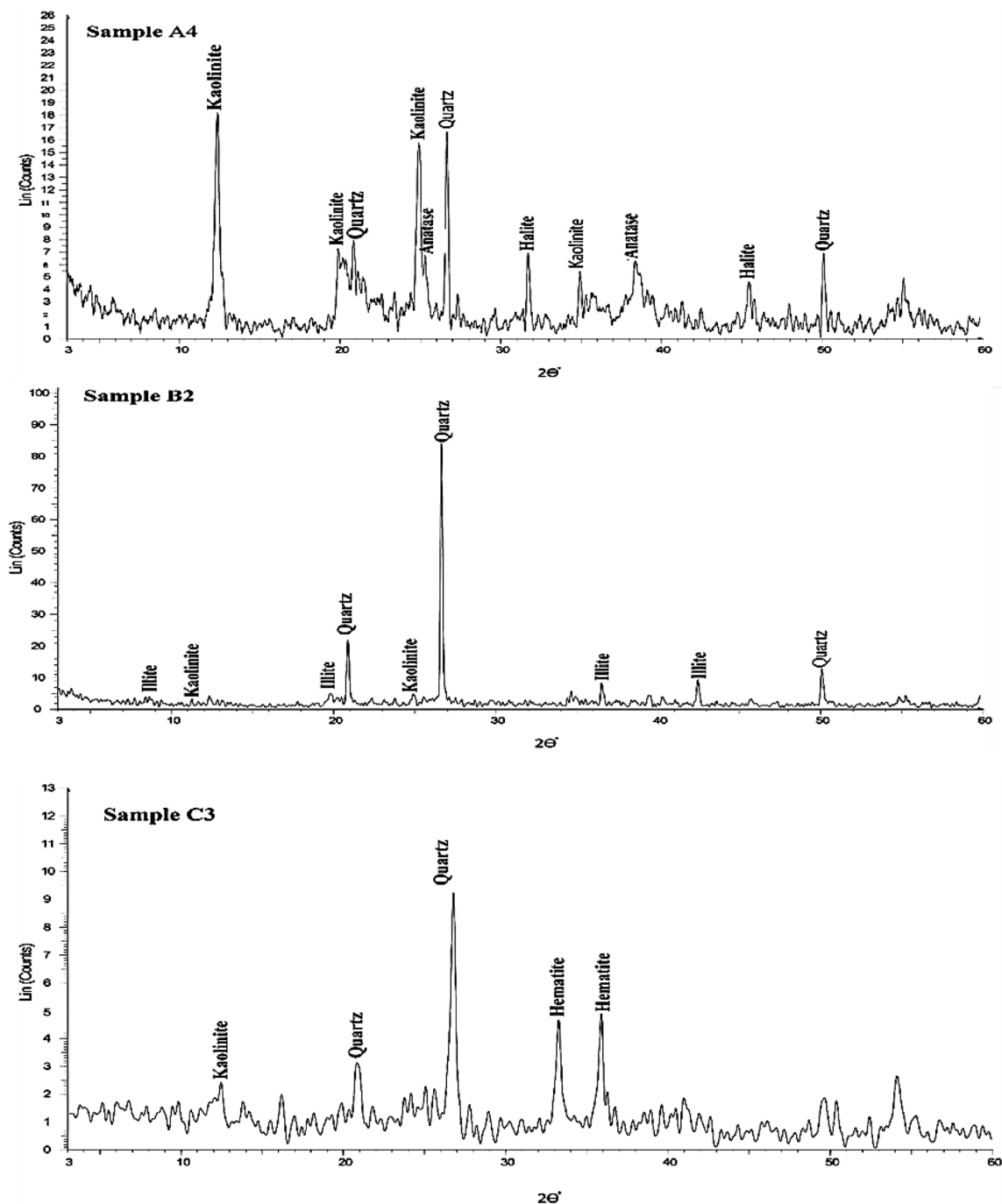


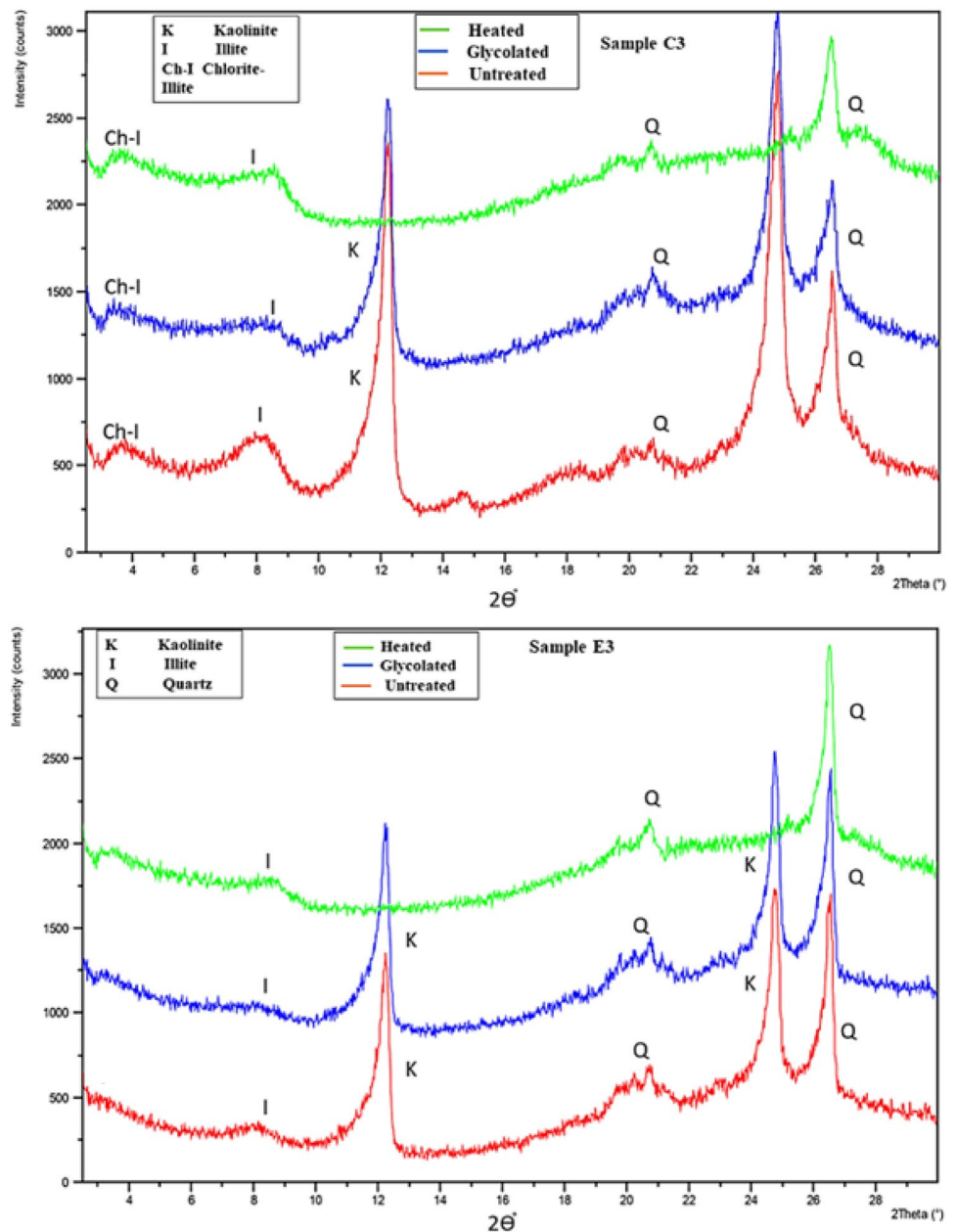
Fig. 5 Selected X-Ray diffraction patterns for the bulk samples of the studied Carboniferous rocks

3.2 Analytical techniques

Five representative lithostratigraphic sections (A to E) of the Carboniferous succession in the study area were measured and thirty-three samples were collected. The sections' locations and distribution of the collected samples are shown in the lithostratigraphic columns (Fig. 3).

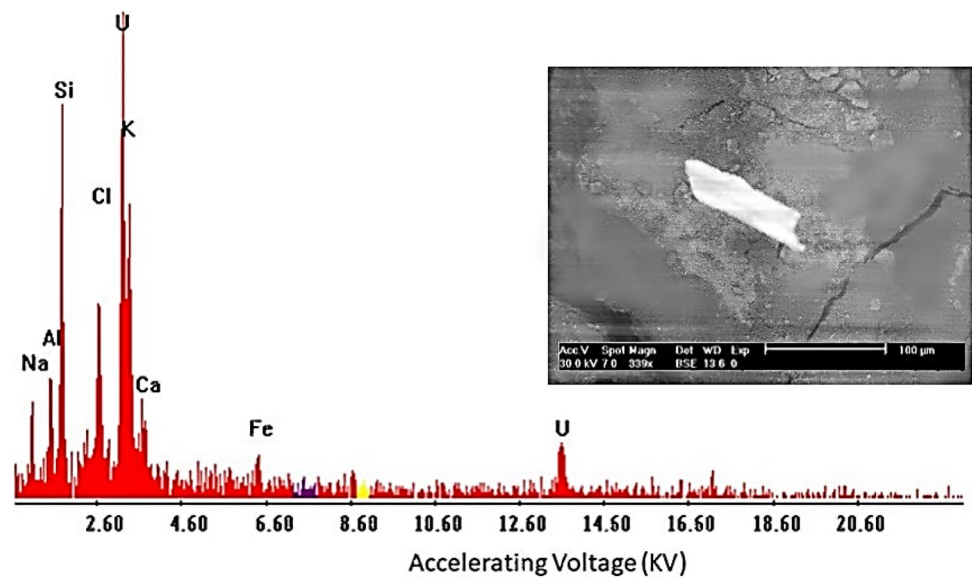
The collected samples were subjected to disaggregation following the procedures described by [27]. Their sand fractions were separated by wet sieving using a 0.63 mm screen. The silt and clay fractions were subjected to pipette analysis to determine their proportions and, consequently, obtain a precise textural nomenclature applying the scheme

Fig. 6 Selected X-Ray diffraction patterns for the clay size fractions of the studied Carboniferous rocks



proposed by [28]. The fine sand and silt size fractions of eight representative samples were used to perform heavy minerals separation using bromoform (sp.g.; 2.85 g/cm³) as described by [29]. The separated heavy minerals were examined microscopically. The bulk and clay mineral compositions of all the collected thirty-three samples were determined using the X-ray Diffraction technique available at the Central Metallurgical Research & Development Institute (CMRDI), Cairo. Instrument settings were adjusted at 40 kV and 40 mA potential, scanning speed of 0.02°/S, and the 2θ ranged between 2 and 60°. The scraped powders of some rock samples were examined using Scanning Electron Microscope attached with Energy energy-dispersive X-ray spectroscopy (EDX) available at the National Research Center (NRC), Egypt. Special attention was given to the spots having yellow colors which might indicate the presence of radioactive minerals. This helped the identification of supergene secondary mineralization and alteration products. REEs analyses for all the collected samples were carried out using Inductively Coupled Plasma Mass Spectrometry (ICP-MS) at ACME Laboratories, Vancouver, Canada.

Fig. 7 BSE image and EDX pattern of uranophane



4 Results and discussion

4.1 Textural and mineralogical compositions

Figure 3 shows the detailed lithologic characteristics of the measured five sections. The studied Carboniferous rocks are entirely clastic and represented by argillaceous and minor arenaceous rocks. Based on their sand, silt and clay contents, these rocks are represented by siltstones, clayey siltstones and, rarely, sandy siltstones and sandstone in the northern part of the study area and claystones in its southern part (Fig. 4). The siltstones are predominantly fissile and laminated. These siltstones dominate all studied five stratigraphic sections. Most likely, these rocks were deposited in shoreline environments represented by lakes and, much less commonly, lagoons. One of the characteristic features of lacustrine sediments is the rhythmic lamination on the scale of millimeters. This type of lamination indicates depositional in quiet waters.

The essential minerals in the studied rocks are quartz and clay minerals. The latter are represented by kaolinite and illite together with minor chlorite-illite mixed layer (Table 2). Figures 5 and 6 show selected XRD patterns of the bulk composition and clay fractions of the studied samples, respectively. The non-radioactive accessory minerals are microcline, gypsum, halite, hematite, anhydrite, barite, pyrite anatase and gibbsite, whereas the radioactive and REEs-bearing minerals are uranophane, xenotime, monazite and zircon.

Uranophane $\text{Ca}(\text{UO}_2)_2(\text{SiO}_3)_2(\text{OH})_2 \times 5\text{H}_2\text{O}$ was found in the scraped powders from the surface of some rock samples. It occurs as yellow euhedral minute crystals, its EDX pattern shows secondary enrichment of iron (Fig. 7). This could be ascribed to Fe proxy for Ca during iron-rich solutions activity phase. Iron proxy for Ca in uranophane was previously reported by several workers [30–32]. Ferrugination of siltstones is another pronounced observation for the effect of iron-bearing solutions. Sources of Fe in these solutions could be the basaltic rocks located close to section C, and/or oxidation of pyrite in siltstones. The formation of this secondary uranium mineral is mainly attributed to the action of oxic groundwater on previously corroded uranium-bearing minerals [33]. The euhedral crystal of uranophane suggests precipitation from the groundwater by evaporation (Fig. 7). The REEs-bearing minerals, on the other hand, could be categorized into primary allogenic and secondary allogenic/ authigenic minerals. The primary REEs-bearing minerals are represented by xenotime, zircon and monazite. Xenotime (YPO₄) occurs as euhedral subrounded crystals (Fig. 8). Its EDX pattern shows the presence of some HREEs such as Yb and Er. Monazite (Ge, La, Nd, Th) (PO₄, SiO₄) exists in the form of detrital grains with pitted surfaces due to weathering. Its REEs contents are dominated by LREEs such as Ce, La, Nd and Sm. Zircon (ZrSiO₄) occurs as prismatic crystals having bipyramidal terminations [34]. Its EDX pattern shows very low REEs contents. Secondary LREEs-bearing minerals were formed on the surfaces of some rocks. Based on their available BSE images and EDX patterns, they are categorized as unidentifiable LREE-bearing silicate minerals (Fig. 8).

Fig. 8 BSE images and EDX patterns of **a** zircon, **b** xenotime, **c** monazite and **d** unidentified LREEs-bearing mineral

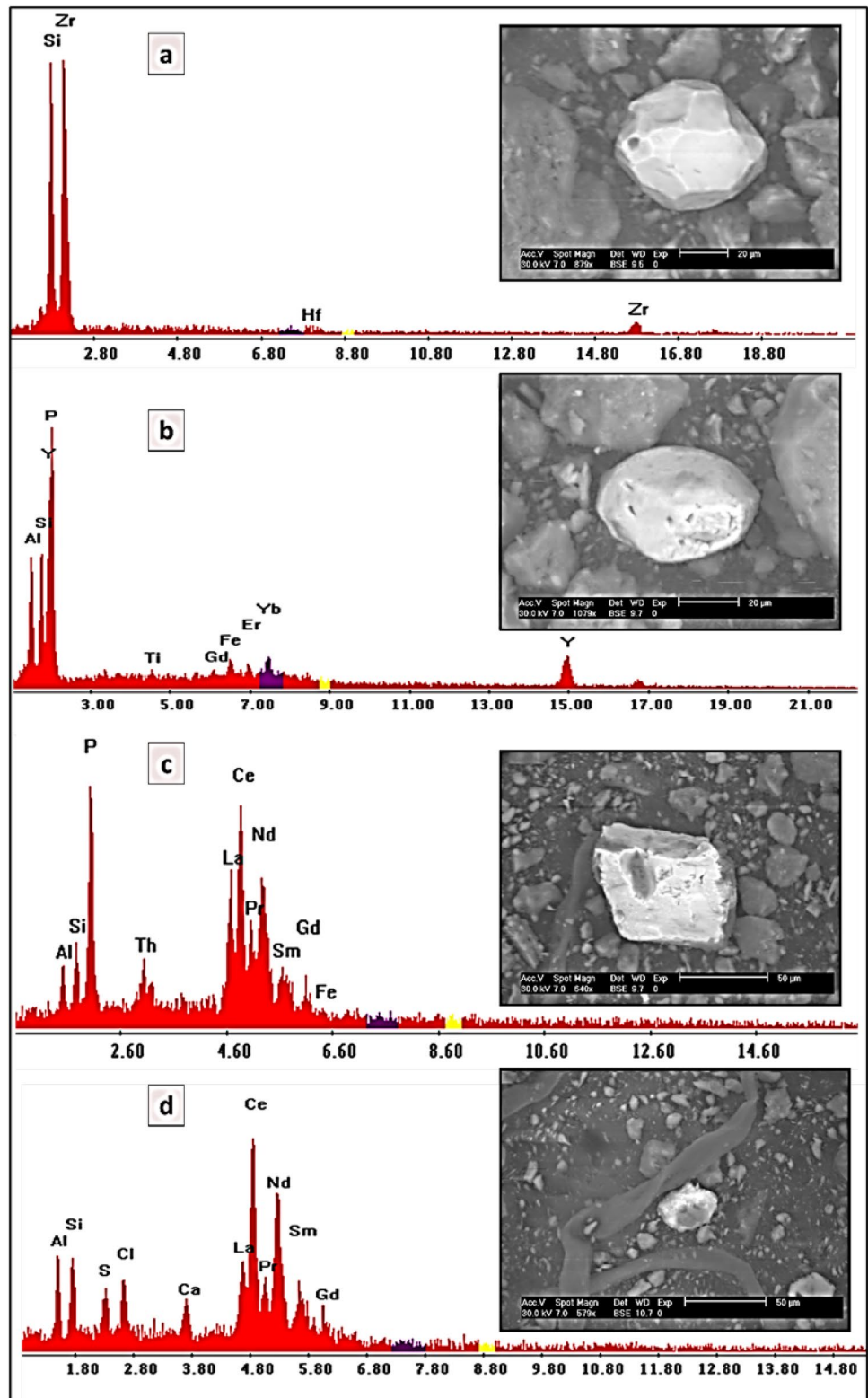


Table 3 Genetic classification of the essential and accessory minerals in the studied Carboniferous rocks

Primary minerals		Secondary minerals	
Allogenic	Authigenic	Allogenic	Authigenic
Kaolinite *	Hematite	Kaolinite	Chlorite-illite
Illite*	Halite	Illite	Gibbsite
Quartz	Barite	Chlorite-illite	Hematite
Zircon	Gypsum	Gibbsite	Xenotime
Monazite	Anhydrite	Hematite	REEs-bearing minerals
Hematite*	Cryptocrystalline silica	Xenotime	
Pyrite	Quartz overgrowths	REEs-bearing minerals	
Barite*	Uranophane		
Anatase			
Xenotime*			
REEs-bearing minerals*			

*Minerals having several possible origins

The types, forms, habits, and modes of occurrence of the minerals in the studied Carboniferous rocks indicate multiple origin being either allogenic or authigenic and primary or secondary (Table 3). The textural and mineral characteristics of the studied rocks indicate inheritance from felsic igneous rocks and, to a much lesser extent, metamorphic and older sedimentary rocks. The limited variations in the clay mineral assemblages among the sections are attributed mostly to the slight differences in the types and the composition of parent rocks. The fact that this detritus is entirely composed of moderately sorted silt and clay particles with occasional minor sand grains indicates that the transporting rivers and streams were of low to moderate strength. Prolonged transportation and contributions from older sedimentary rocks could be confirmed by the relative high roundness degree of silt and sand grains and the markedly low proportions of rock fragments.

4.2 REEs geochemistry

The concentrations of the REEs in the studied Carboniferous rocks are listed in Tables 4, 5, 6. These rocks have low to moderate total REEs concentrations. The lowest Σ REEs value (2.84 ppm) was found in the sandy siltstone of section A whereas the highest value (163.24 ppm) was reported in the clayey siltstone of section C. Quartz and clay minerals are the essential minerals in the bulk samples (Table 2, Fig. 5). The REEs contents of quartz are known to be very low, [35, 36]. This explains the markedly low contents of REEs in the coarser sediments (Section A, Table 4). Conversely, clay minerals are important hosts of REEs [37] which resulted in the enrichment of REEs in the fine-grained sediments (Sections C, D, and E). The adsorption mechanisms of REEs to clays remain unclear and the adsorbed state of REEs has never been demonstrated in situ [38].

The highest Σ REEs value was reported in sample C7 which was collected from rocks close to the contact with the Oligocene basalt. The REEs enrichment in these rocks is most probably attributed to the effect of the hydrothermal solutions that accompanied volcanic activity. Rocks of the southern section's D and E have higher REEs contents than those of the other sections (Fig. 9). This could be attributed to the presence of gibbsite. Gibbsite-bearing shale has been identified as containing physically adsorbed rare earth elements [39, 40]. The basic structure of gibbsite is made up of stacked sheets of linked octahedra. This structure probably provides spaces for REEs adsorption. Therefore, it could be concluded that the REEs contents of the Carboniferous rocks in the study area increase significantly southward accompanying the increase of clay contents, gibbsite, and alteration.

The REEs patterns for the studied rocks were normalized to those of the Chondrite and Post-Archean Australian Average Shale (PAAS) (Figs. 10, 11). Except for samples of section A that have very low REEs contents, those of the other sections have REEs enriched patterns with negative Eu anomalies which may be attributed to the non-significant plagioclase content of the rocks and/or the removal of Eu by alteration processes. The average values of Δ Eu are 0.38, 0.52, 0.54, 0.59, and 0.58 in sections A, B, C, D, and E; respectively.

The REEs in the studied samples are dominated by LREEs (average 62 ppm) as compared with the HREEs (average 6.23 ppm). The REEs patterns indicate distinct fractionation of HREEs where the average (Gd/Yb)_N value is 8.03. In contrast, the LREEs show relatively weak fractionation with an average (La/Yb)_N value of 0.64 (Tables 4, 5, 6). The ratio of LREE/

Table 4 Concentrations (ppm) of the rare earth elements in the Carboniferous rocks of sections A, B & C

S.N	A1	A3	A4	B1	B2	B4	B6	B7	C1	C2	C3	C4	C5	C6	C7
R.T	St.	Sandy St.	Sandy St.	St.	St.	St.	St.	St.	St.	St.	Clayey St.	St.	St.	Clayey St.	Clayey St.
La	6.4	0.5	0.7	30.6	24.1	11.5	13.5	29.9	18.2	10.1	27.1	20.2	21.4	25.3	67
Pr	4.72	0.13	0.25	7.92	6.18	3.59	4.05	9.53	6.01	3.2	8	6.71	6.79	8.17	16.06
Nd	24.55	0.61	1.18	30.3	23.03	13.5	15.25	36.2	22.54	12.94	28.59	24.04	26.39	32.2	54.95
Sm	6.59	0.24	0.24	5.83	4.69	2.53	2.89	6.62	4.51	3.46	5.03	4.73	4.73	7.14	10.27
Eu	1.35	0.05	0.05	0.84	0.78	0.29	0.56	1.18	0.72	0.69	0.78	0.68	0.74	1.14	0.81
Gd	4.44	0.26	0.16	4.51	4.34	1.66	2.05	4.35	2.67	3.66	3.02	3.13	2.85	5.65	7.21
Tb	0.54	0.05	0.02	0.5	0.48	0.18	0.27	0.42	0.28	0.37	0.31	0.33	0.27	0.55	0.92
Dy	2.25	0.45	0.11	2.02	1.9	0.76	1.22	1.57	1.09	1.36	1.44	1.31	1.05	2.07	3.84
Ho	0.28	0.1	0.02	0.25	0.27	0.13	0.19	0.15	0.12	0.16	0.2	0.16	0.1	0.24	0.54
Er	0.72	0.25	0.03	0.48	0.64	0.31	0.43	0.31	0.28	0.31	0.51	0.36	0.26	0.46	1.02
Tm	0.09	0.04	0.02	0.05	0.06	0.03	0.06	0.03	0.03	0.03	0.07	0.03	0.02	0.05	0.09
Yb	0.45	0.21	0.04	0.32	0.32	0.18	0.37	0.23	0.18	0.18	0.43	0.18	0.14	0.28	0.49
Lu	0.05	0.03	0.02	0.03	0.04	0.03	0.04	0.02	0.03	0.02	0.04	0.02	0.02	0.04	0.04
ΣREEs	52.43	2.92	2.84	83.65	66.83	34.69	40.88	90.51	56.66	36.48	75.52	61.88	64.76	83.29	163.24
LREE/HREE	4.94	1.10	5.76	9.25	7.30	9.58	7.83	11.78	11.11	4.99	11.54	10.21	12.75	7.92	10.54
δEu	0.84	0.15	0.16	0.54	0.53	0.29	0.52	0.74	0.56	0.53	0.57	0.50	0.56	0.66	0.40
(La/Yb)N	1.05	0.18	1.29	7.05	5.55	4.71	2.69	9.58	7.45	4.13	4.64	8.27	11.26	6.66	10.08
(La/Sm)N	0.14	0.31	0.43	0.77	0.76	0.67	0.69	0.66	0.59	0.43	0.79	0.63	0.67	0.52	0.96
(Gd/Yb)N	5.88	0.74	2.38	8.39	8.08	5.49	3.30	11.27	8.84	12.11	4.18	10.36	12.12	12.02	8.76

R.T. Rock type, St. Siltstone

Table 5 Concentrations (ppm) of rare earth elements in the Carboniferous rocks of section D

S.N	D1	D2	D3	D4	D5	D6	D7	D8	D9	D10
R.T	Clayey St.	St.	St.	St.	Clayey St.	St.	St.	Cl.	Clayey St.	Clayey St.
La	26.3	21.1	27.3	23.5	28.7	24.5	25.1	23.2	20.3	23.8
Pr	8.67	6.94	8.51	7.29	8.96	7.41	8.18	7.49	6.89	7.72
Nd	35.65	26.5	30.08	26.73	32.99	27.56	29.29	27.26	25.94	27.11
Sm	8.11	5.8	4.78	5.04	6.34	4.71	5.03	4.63	5.08	5.46
Eu	1.52	0.94	0.71	0.77	0.9	0.66	0.82	0.71	0.8	0.78
Gd	7.12	4.67	2.77	3.26	3.66	2.48	3.21	2.66	3.35	3.1
Tb	0.85	0.5	0.28	0.35	0.31	0.25	0.33	0.27	0.38	0.34
Dy	3.12	1.9	1.04	1.32	1.21	0.91	1.25	0.95	1.45	1.29
Ho	0.39	0.26	0.11	0.18	0.11	0.12	0.13	0.13	0.19	0.14
Er	0.67	0.54	0.23	0.35	0.19	0.28	0.37	0.27	0.36	0.27
Tm	0.07	0.06	0.03	0.04	0.03	0.03	0.04	0.03	0.04	0.03
Yb	0.41	0.38	0.19	0.27	0.21	0.24	0.2	0.19	0.24	0.18
Lu	0.04	0.04	0.02	0.03	0.03	0.02	0.03	0.02	0.04	0.02
ΣREEs	92.92	69.63	76.05	69.13	83.64	69.17	73.98	67.81	65.06	70.24
LREE/HREE	6.33	7.34	15.28	10.92	13.55	14.97	12.31	14.00	9.75	12.08
δEu	0.80	0.60	0.54	0.55	0.59	0.51	0.59	0.55	0.57	0.55
(La/Yb)N	4.73	4.09	10.59	6.41	10.07	7.52	9.25	9.00	6.23	9.74
(La/Sm)N	0.48	0.54	0.84	0.69	0.67	0.77	0.74	0.74	0.59	0.64
(Gd/Yb)N	10.35	7.32	8.69	7.19	10.38	6.16	9.56	8.34	8.32	10.26

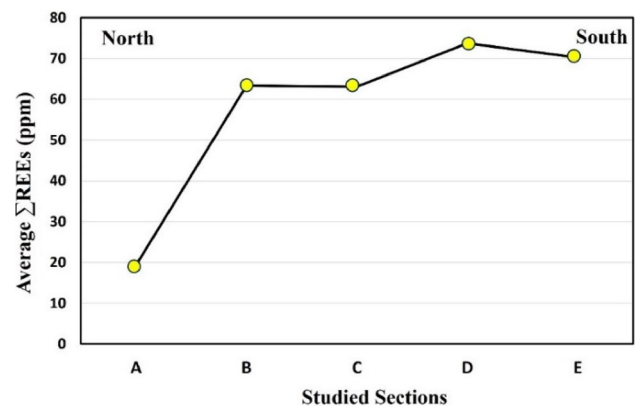
R.T. Rock type, St. Siltstone, Cl. Claystone

Table 6 Concentrations (ppm) of the rare earth elements in the Carboniferous rocks of section E

S.N	E1	E2	E3	E4	E5	E6	E7	E8
R.T	St.	Clayey St.	St.	Clayey St.	St.	St.	St.	St.
La	15.4	27.9	21.9	26	24.5	22.1	29.7	15.3
Pr	4.15	10.24	6.82	8.69	8.05	7.04	9.31	4.56
Nd	15.14	39	25.87	33.14	29.52	26.84	35.1	17.26
Sm	2.89	8.09	5.54	5.25	5.4	4.87	6.68	3.1
Eu	0.48	1.33	0.9	0.79	0.78	0.83	1.1	0.44
Gd	1.61	5.13	4.06	3.38	3.45	3.36	4.33	2.17
Tb	0.16	0.62	0.43	0.31	0.35	0.36	0.5	0.24
Dy	0.65	2.48	1.86	1.19	1.24	1.38	2.21	1
Ho	0.07	0.29	0.25	0.12	0.15	0.16	0.26	0.15
Er	0.17	0.67	0.49	0.3	0.32	0.31	0.53	0.31
Tm	0.02	0.06	0.06	0.03	0.03	0.04	0.05	0.04
Yb	0.14	0.42	0.33	0.18	0.21	0.23	0.42	0.23
Lu	0.02	0.04	0.04	0.02	0.03	0.02	0.04	0.02
ΣREEs	40.9	96.27	68.55	79.4	74.03	67.54	90.23	44.82
LREE/HREE	13.40	8.91	8.12	13.36	11.81	10.53	9.82	9.77
δEu	0.47	0.76	0.60	0.56	0.54	0.60	0.69	0.40
(La/Yb)N	8.11	4.89	4.89	10.64	8.60	7.08	5.21	4.90
(La/Sm)N	0.79	0.51	0.58	0.73	0.67	0.67	0.66	0.73
(Gd/Yb)N	6.85	7.28	7.33	11.19	9.79	8.70	6.14	5.62

R.T. Rock type, St. Siltstone

Fig. 9 The average Σ REEs distribution in the rocks of the study area



HREE reveals the fractionation between LREEs and HREEs in the rocks. The average LREE/HREE ratios are 3.93, 9.15, 9.87, 11.65, and 10.75 in sections A, B, C, D, and E; respectively. Previous studies have indicated that progressive weathering fractionates REEs and, therefore, the weathering products are commonly more enriched in LREEs than in HREEs [41, 42]. The marked dominance of kaolinite in the rocks of the study area (Table 2) might have contributed to the high REEs contents in their clay fractions. Nesbitt [43] deduced that kaolinite is more able to accommodate LREEs. Braun et al. [44] concluded that, when mobilized, LREEs may be incorporated in the secondary REEs-bearing phases and absorbed into the clay particles. This conforms well with the occurrence of secondary LREEs-bearing minerals on the surfaces of the studied rocks (Fig. 8). This preferential mobility of LREEs may explain their high contents in the studied rocks.

4.3 Remote sensing analysis

The digital number (DN) value of pixels corresponding to sampling sites in each band was converted to spectral reflectance. The rocks with relatively high REEs contents exhibit spectral traits that are different from rocks with low REEs. The spatial distribution of REEs shows a high REEs trend toward the south of the study area at (Sections C, D, and E) (Fig. 12).

4.3.1 Geographic distribution of REE by GIS.

The spatial distributions of the individual REEs in the Carboniferous rocks of the study area show the same pattern as that of the total REEs (Fig. 13). This implies a similar REEs behavior in different geochemical interactions [46]. On the contrary, uranium spatial distribution shows dissimilar patterns. This dissimilarity is related to different sources of REEs and uranium in the rocks.

4.3.2 Alteration zones detection and minerals discrimination

PCA bands 1, 2, and 3 for R, G, and B; respectively, are the most useful as they show the greatest amount of variation enabling discrimination of the different rock units. Decorrelation of b8-b7-b6 enhances color differences in any false color multispectral satellite images. It reduces the highly correlated bands to discriminate the different rock units and to show the high alteration in blue color. The two analyses indicate an association of alteration products and REEs-bearing parts of the rocks (Fig. 14).

Regarding the multitude of components that comprise the studied rocks, REEs existence is generally uncertain. As a result, a direct estimation of the REEs contents of the rocks based only on the spectra is difficult. However, alteration products such as hydroxyl (OH) mineral group, clays, kaolinite, illite, and muscovite exhibit significant absorption at SWIR (from 1600 to 2430 nm) which may offer an additional indication of REEs distributions. The ratio image of ASTER (B6/B4, B7/B3, B3/B1 in R, G, B) distinguishes between the altered zones (pale red) and non-altered zones (Fig. 15a). The clay minerals ratio (B1–B7)/(B6–B6) is used to emphasize the clay minerals content as indirect indication for the distribution of REEs in the rocks [47]. The clay alteration index map indicates the presence of alteration zones with high clay contents that appear in green color slicing. These clay alteration zones are parallel to the NW–SE trend of the major Gulf of Suez rift (Fig. 15b). These zones are also characterized by kaolinization

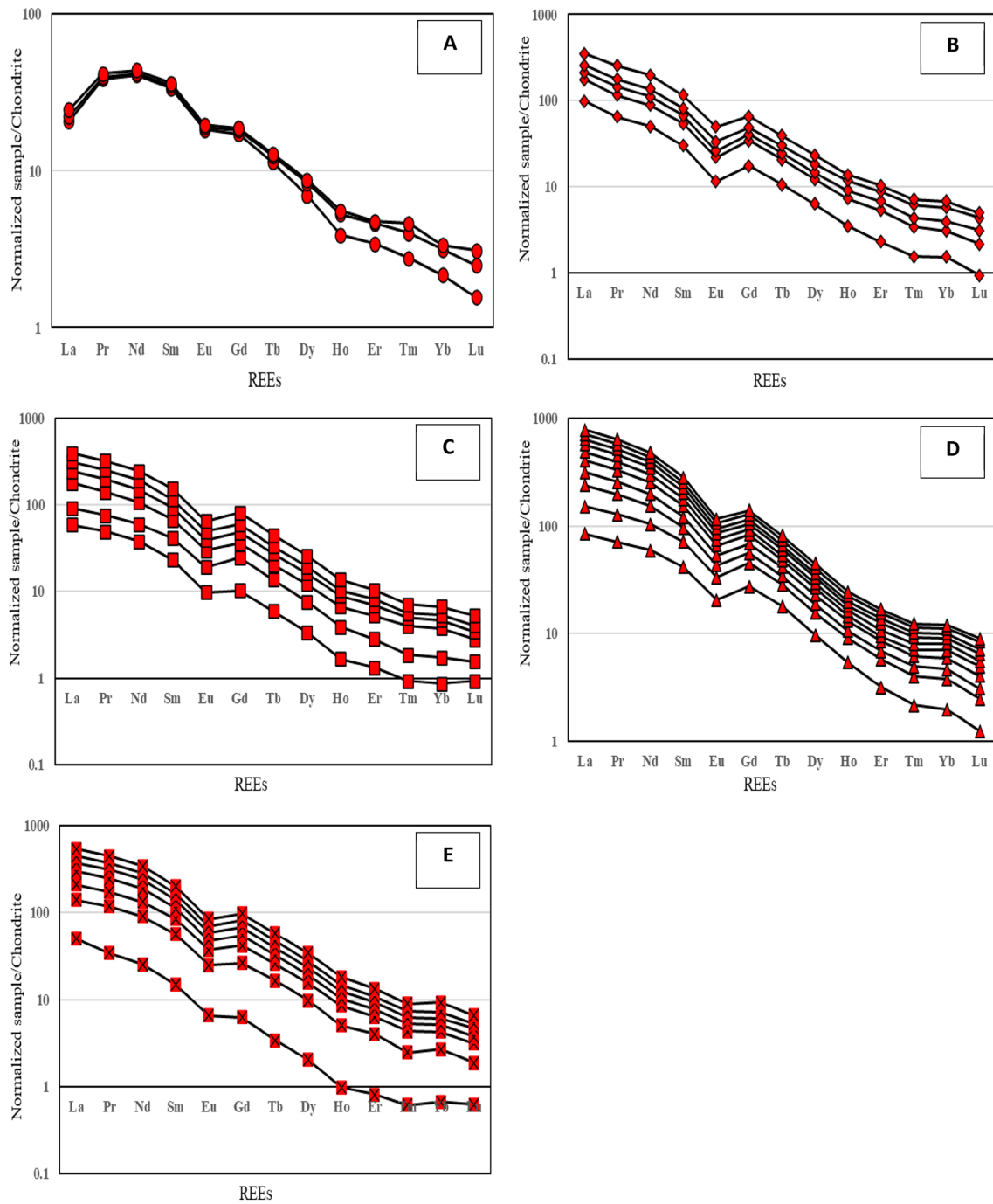


Fig. 10 REEs patterns for rocks of sections **A**, **B**, **C**, **D** and **E** normalized to those of the chondrite as given by [45]

that appears in pale blue color slicing (Fig. 15c). Hydroxyl ion as an indication for clays and other sheet silicates has spectral significance at 1.4 and 2.3µm. The band math ((B7/B6) * (B4/ B6)) was used to highlight the spectral response and separate the alteration zones rich in hydroxyl ion shown as yellow slicing color (Fig. 15d). These

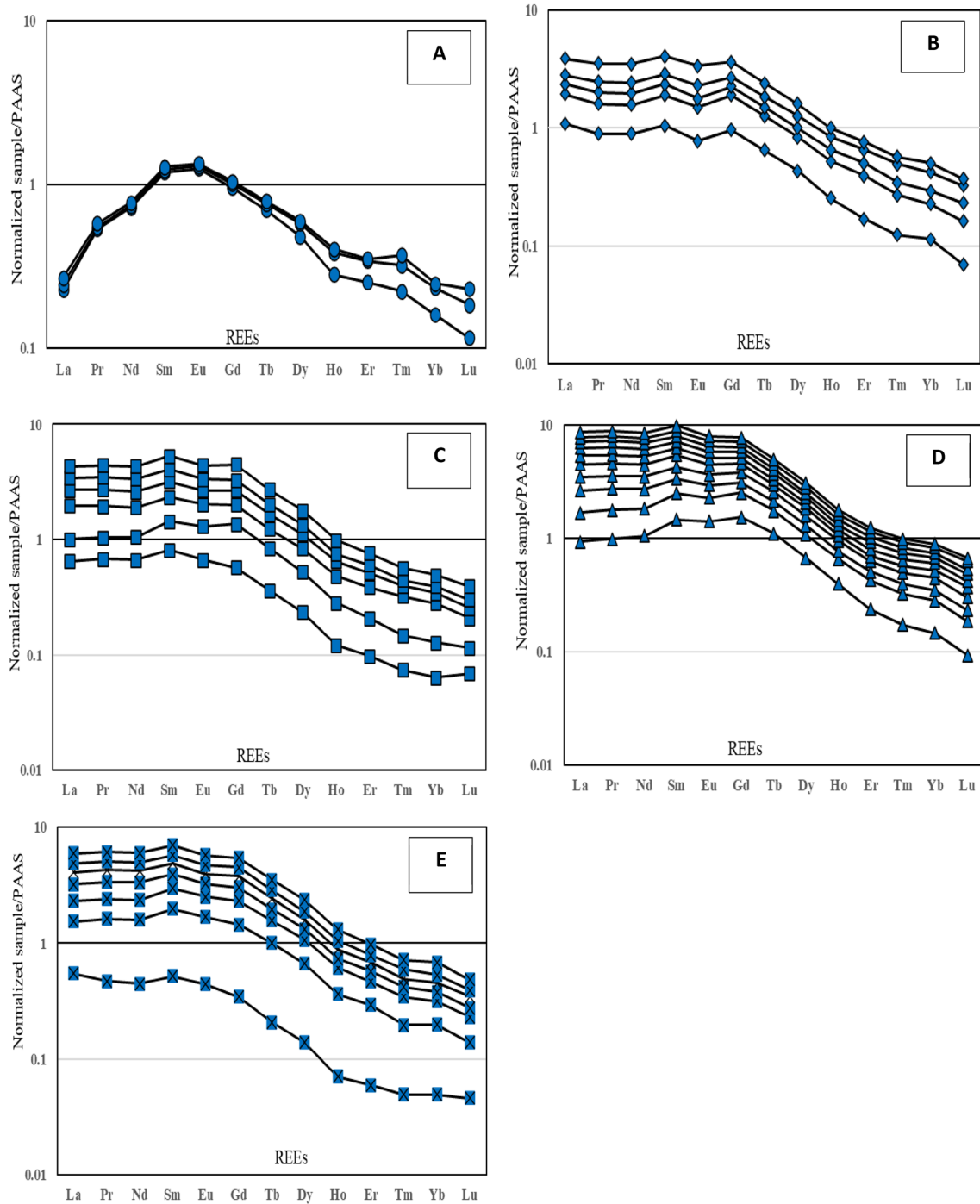
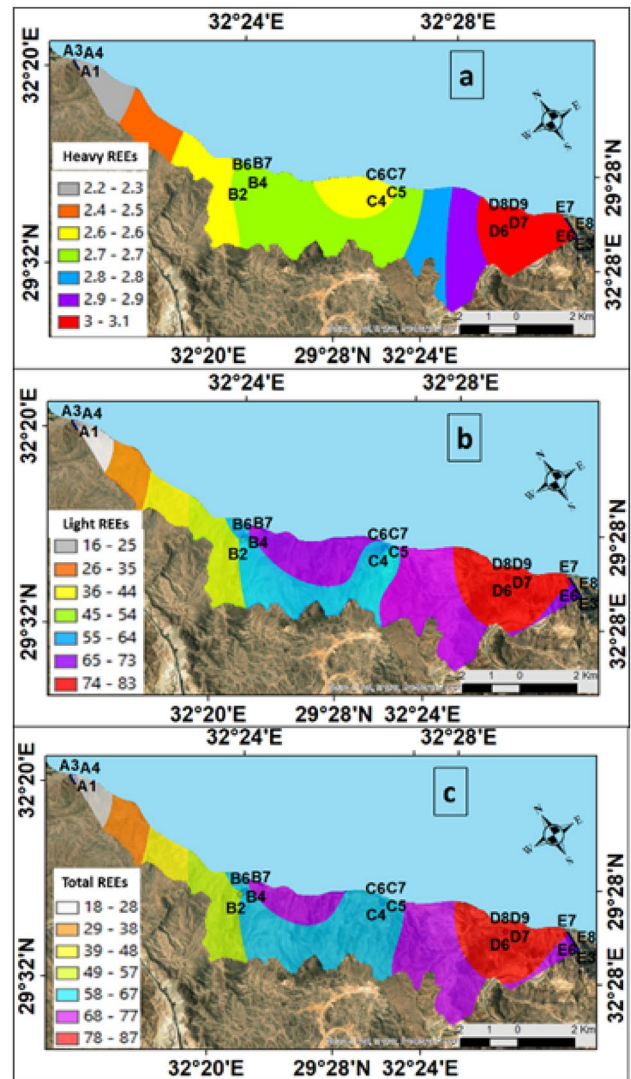


Fig. 11 REEs patterns for rocks of sections **A**, **B**, **C**, **D** and **E** normalized to those of the PAAS as given by y[45]

zones are almost overlapped with the alteration, clays, and kaolinite zones (Fig. 16a–c). The (CO_3^-) –epidote has a prominent absorption peak at 2.3 μm with $((B7 + B9)/B8)$ ratio. It is shown as violet color slicing and can be used to discriminate the rock with a high abundance of CO_3^- –epidote (Fig. 15e). Muscovite distribution is shown as

Fig. 12 **a** HREEs, **b** LREEs, and **c** Total REEs, spatial distribution in the Carboniferous rocks of the study area based on field observations and geochemical analysis overlaid on the true color satellite image



pink slicing color overlapping the hydroxyl ion alteration zones (Fig. 15f), the red color slicing used to discriminate the rock with a high abundance of illite (Fig. 15g). The Pale-yellow color slicing discriminates the rock with a high abundance of amphibole (Fig. 15h) is generally not interfering with REEs distribution.

Band algebra $(B8 + B7/B6)$ and $(B4 + B6/B5)$ were created to map the low REEs contents of the rocks and other $(B5 + B7)/B6$ and $(B7/B6) * (B4/B6)$ to map the high REEs contents (Fig. 15i). This figure shows that the distribution of REEs overlapped with the alteration zones represented mainly by clays, kaolinite and hydroxyl ion. The high distribution occurs mainly in the southern part of the study area.

4.3.3 Surface lineament interpretation

Enhancement, filtering procedures, and PCA were implemented to enhance the visual look of the satellite image and prepare it for feature and structural measurements (Fig. 16a). The image properties, lithological boundaries, and geomorphological aspects were used to extract lineaments and visual interpretation criteria. The distribution of alteration

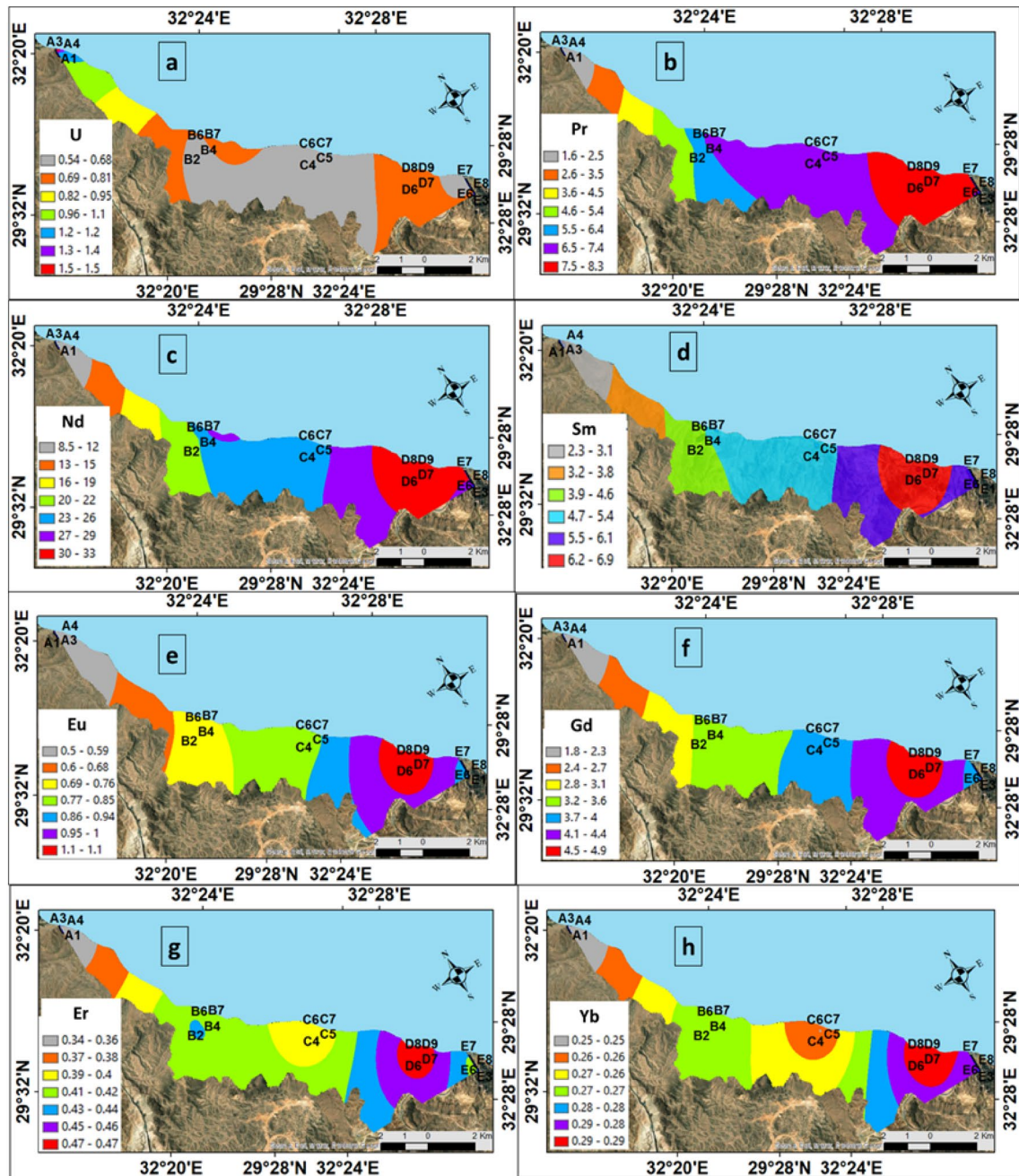


Fig. 13 Spatial distributions of **a** uranium (U), some individual REEs: **b** Pr, **c** Nd, **d** Sm, **e** Eu, **f** Gd, **g** Er, and **h** Yb in the Carboniferous rocks of the study area based on field sampling and geochemical analysis overlaid on the true color satellite image

Fig. 14 **a** Principal component analysis (PC1, PC2, and PC3 in RGB) (REEs in yellow color), and **b** Decorrelation stretch for B8, B7, and B6 (alteration products in blue color)

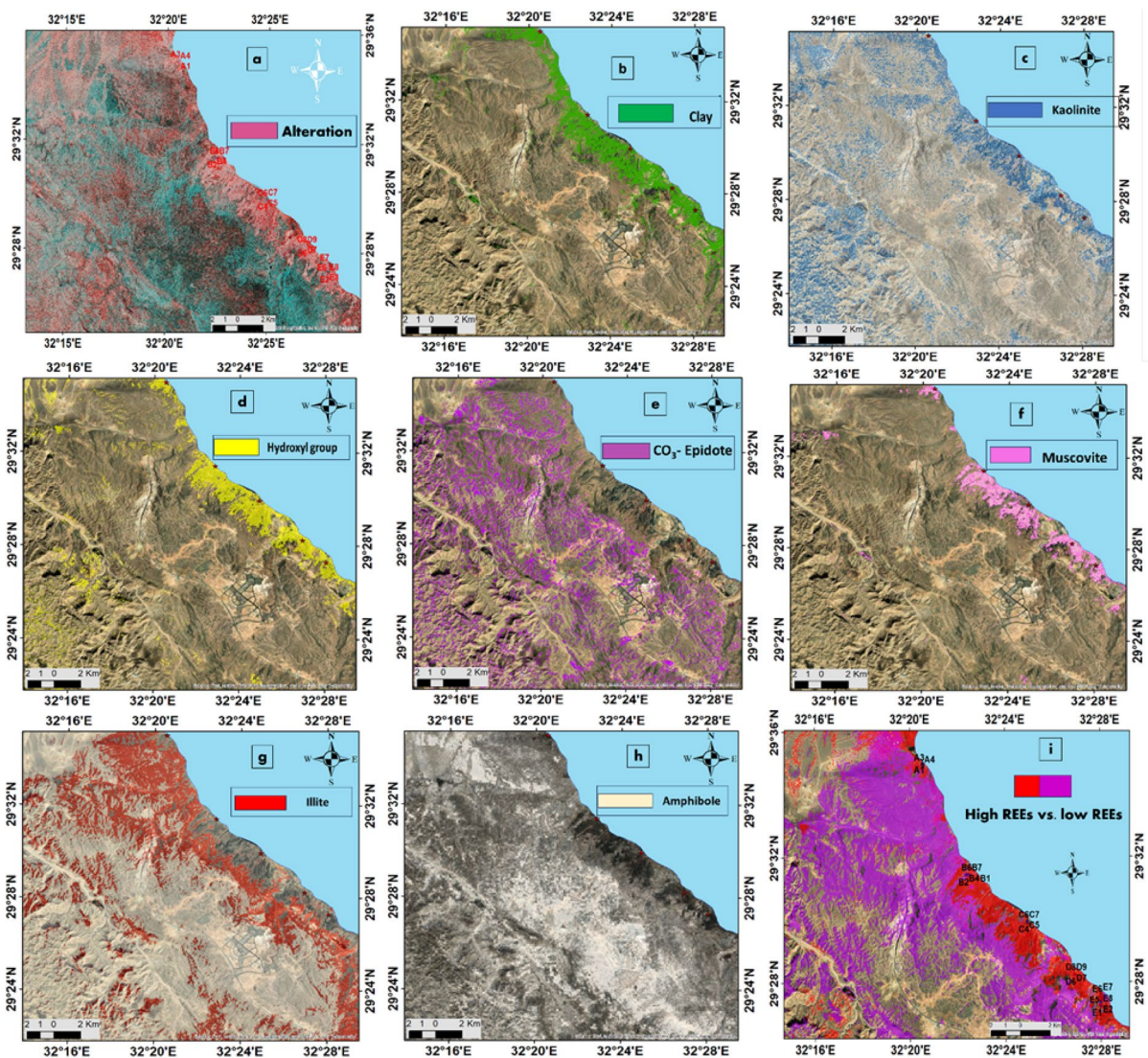
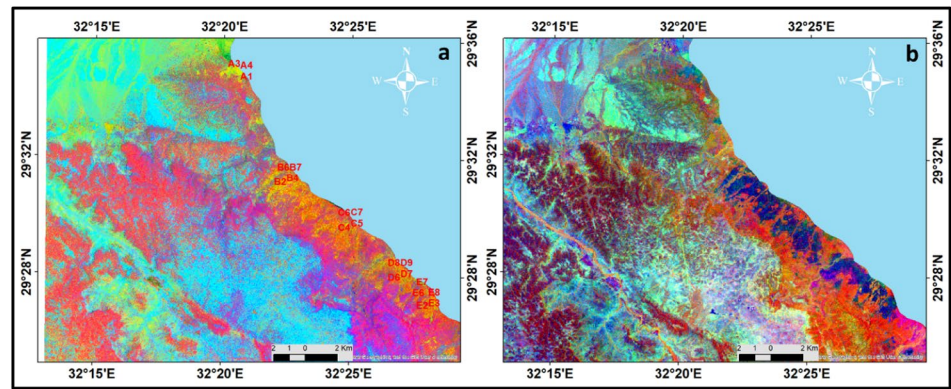


Fig. 15 Alteration product slices from the different band algebra overlaid on the true-color satellite image of the study area

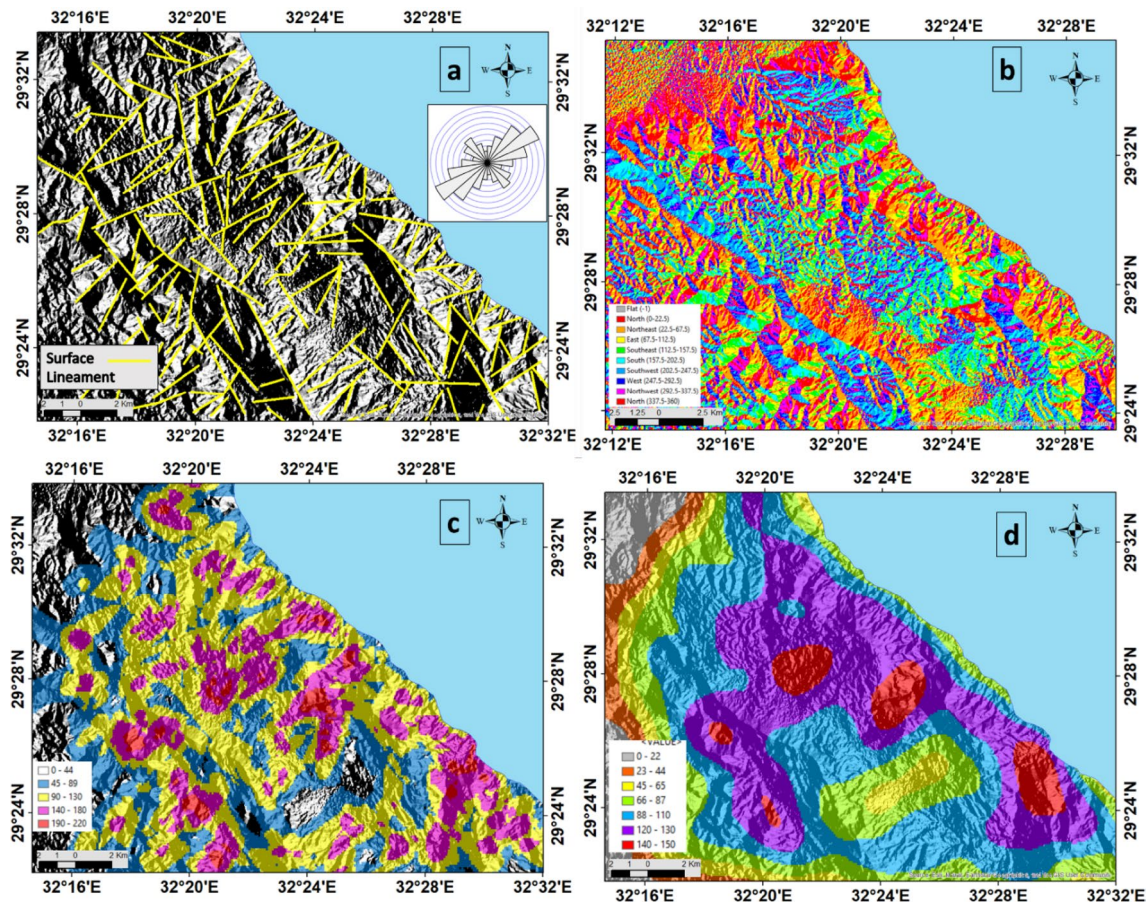


Fig. 16 **a** Surface lineament derived from various lineament extraction remote sensing techniques with its rose diagram. **b** Slope-aspect map of the study area. **c** Surface lineament density map derived from satellite image and **d** Kernel lineament density

products was governed by the collective action of tectonic settings and slope aspect (Fig. 16b). In the study area, structural lineaments have four mapped primary fault trends: NW, NE, N–S, and ENE. The slope direction controls the runoff transfer of sediments and mobile elements in the rocks. The spatial distribution of REEs in the Carboniferous rocks of the study area was assessed using altitude, slope-aspect, and structural controls. Higher lineament density zones are observed in the rocks having higher contents of REEs (Fig. 16c, d).

5 Conclusions

The Carboniferous rocks in the eastern part of El Galala El Bahariya plateau are represented by siltstones and, rarely, sandy siltstones and sandstones in the northern part of the study area and claystones in its southern part. These rocks are composed mainly of quartz and clay minerals; the latter are represented by kaolinite and subordinate illite together with minor chlorite-illite mixed layer. The accessory non-radioactive minerals are microcline, gypsum, anhydrite, halite, barite, hematite, pyrite, anatase, and gibbsite. On the other hand, the radioactive and REEs-bearing minerals are uranophane, xenotime, monazite, and zircon. The types, forms, habits, and modes of occurrence of the recorded minerals indicate a multiple origin being either allogenic or authigenic and primary or secondary.

The REEs in the studied rocks generally show enriched patterns with -ve Eu anomaly. This anomaly is attributed to the insignificant plagioclase content of the rocks and/or the removal of Eu by alteration processes. The fact that the REEs contents of quartz are known to be very low explains their markedly low concentrations in the coarser sediments of the northern part of the study area. Conversely, clay minerals and gibbsite are important hosts of REEs,

this explains the highest concentrations of REEs in the clay-rich rocks of the southern part of the study area. When mobilized, LREEs are incorporated in secondary REEs-bearing phases and adsorbed onto clays. This preferential mobility of LREEs explains the high LREE/HREE ratios in the studied rocks.

Applying several remote sensing techniques revealed that the structural lineaments in the study area have four mappable primary fault trends. Enhancement, filtering procedures, and PCA were implemented to enhance the visual look of the satellite image and prepare it for structural measurements. The NW–SE, N–S, and NE–SW faults structurally controlled the distribution of REEs and alteration zones. The ASTER band ratio images distinguished between the argillic and non-argillic mineral indicators and illite, Kaolinite, alunite, sericite, and epidote mineral indicators. Bands math, density mapping, and slicing applications were used to link the output results and REE potentiality sites. Different bands algebra was created to map the low and the high REEs contents of the rocks. The rocks with relatively high REEs contents exhibit spectral traits that are different from rocks with low REEs. The alteration zones are linked with the clay minerals abundance, the REEs concentrations, and high lineament structure density. According to the spatial distribution map of the REEs, their highest concentrations appeared in the southern part of the study area.

Acknowledgements Not applicable.

Author contributions All the authors contributed to the study. Randa S. Ramadan, Yehia H. Dawood, and Shaimaa M. El-hadidy wrote the manuscript and prepared figures. Mohamed M. Abu-zeid, Ashraf R. Baghdady and Ahmed Gad reviewed and edited the main manuscript text. All authors reviewed the manuscript.

Funding The authors have no relevant financial or non-financial interests to disclose. This study did not receive any funding in any form.

Data availability Data “available on request”, remote sensing is Open data and content can be freely used, modified, and shared by anyone for any purpose” and all links were written in the manuscript.

Data is contained within the article, remote sensing is open data and content can be freely used, modified, and shared by anyone for any purpose”. All relevant links are provided within the manuscript, and any Data is “available on request”.

Code availability Not applicable.

Declarations

Ethics approval and consent to participate Not applicable.

Consent for publication All authors gave their consent to publish this article.

Competing interests Competing interest on behalf of all authors, the corresponding author states that the authors have no competing interests to declare that are relevant to the content of this article.

Open Access This article is licensed under a Creative Commons Attribution 4.0 International License, which permits use, sharing, adaptation, distribution and reproduction in any medium or format, as long as you give appropriate credit to the original author(s) and the source, provide a link to the Creative Commons licence, and indicate if changes were made. The images or other third party material in this article are included in the article’s Creative Commons licence, unless indicated otherwise in a credit line to the material. If material is not included in the article’s Creative Commons licence and your intended use is not permitted by statutory regulation or exceeds the permitted use, you will need to obtain permission directly from the copyright holder. To view a copy of this licence, visit <http://creativecommons.org/licenses/by/4.0/>.

References

1. Kontinen A, Hanski E. The talvivaara black shale-hosted Ni-Zn-Cu-Co deposits in eastern Finland. Amsterdam: Elsevier; 2015. <https://doi.org/10.1016/B978-0-12-410438-9.00022-4>.
2. Armostrong JGT, Paraneil J, Bullock L, Boyce A, Perez M, Feldmann J. Mobilization of arsenic, selenium and uranium from carboniferous black shales in west Ireland. *Appl Geochem*. 2019;109: 104401. <https://doi.org/10.1016/j.apgeochem.2019.104401>.
3. Fang C, et al. Geological significance of rare earth elements in marine shale of the upper permian dalong formation in the Lower Yangtze Region, South China. *Minerals*. 2023. <https://doi.org/10.3390/min13091195>.
4. Eker CS, Sipahi F, Kaygusuz A. Trace and rare earth elements as indicators of provenance and depositional environments of Lias cherts in Gumushane, NE Turkey. *Geochemistry*. 2012;72:167–77. <https://doi.org/10.1016/j.chemer.2011.11.004>.
5. Ma L, Jin L, Brantley SL. How mineralogy and slope aspect affect REE release and fractionation during shale weathering in the Susquehanna/Shale Hills Critical Zone Observatory. *Chem Geol*. 2011;290(1):31–49. <https://doi.org/10.1016/j.chemgeo.2011.08.013>.
6. Cao XD, Chen Y, Wang XR, Deng XH. Effects of redox potential and PH value on the release of rare earth elements from soil. *Chemosphere*. 2001;44:655–61. [https://doi.org/10.1016/S0045-6535\(00\)00492-6](https://doi.org/10.1016/S0045-6535(00)00492-6).

7. Davranche M, Pourret O, Gruau G, Dia A, Le Coz-Bouhnik M. Adsorption of REE(III)-humate complexes onto MnO₂: experimental evidence for cerium anomaly and lanthanide tetrad effect suppression. *Geochim Cosmochim Acta*. 2005;69:4825–35. <https://doi.org/10.1016/j.gca.2005.06.005>.
8. Mihajlovic J, Rinklebe J. Rare earth elements in German soils—a review. *Chemosphere*. 2018;205:514–23. <https://doi.org/10.1016/j.chemosphere.2018.04.059>.
9. Laakso K, Turner DJ, Rivard B, Sánchez-Azofeifa A. The long-wave infrared (8–12 μm) spectral features of selected rare earth element—bearing carbonate, phosphate and silicate minerals. *Int J Appl Earth Obs Geoinf*. 2019;76:77–83. <https://doi.org/10.1016/j.jag.2018.11.005>.
10. Booyesen R, Jackisch R, Lorenz S, Zimmermann R, Kirsch M, Nex PA, Gloaguen R. Detection of REEs with lightweight UAV-based hyperspectral 868 imaging. *Sci Rep*. 2020;10(1):1–12. <https://doi.org/10.1038/s41598-020-74422-0>.
11. Amer R, Kusky TM. Aster analysis for locating REE-bearing granites in arid regions: example from the Arabian Shield. *J Earth Sci*. 2020;33(5):1114–23. <https://doi.org/10.1007/s12583-022-1650-0>.
12. Schweinfurth G. Sur la découverte d'une faune Paléozoïque dans le grès d'Égypte. *Bull Inst de l'Égypte*. 1883;6(2):239–55. <https://doi.org/10.11588/diglit.9038.15>.
13. Said R. Explanatory notes to accompany the geological map of Egypt. *Egypt Geol Surv*. 1971;56:123.
14. Abdallah A, El-Adindani A. Stratigraphy of the Upper Paleozoic rocks. Western side of the Gulf of Suez Geological Survey, Mineralogical Resources Department, vol. 25. Cairo, Egypt; 1963. p. 1–18.
15. Beleity AM, Ghoneim M, Hinawi M, Fathi M, Gebali H, Kamel M. Paleozoic stratigraphy, paleogeography and paleo tectonics in the Gulf of Suez. In: 8th exploration conference E. G.P.C., Cairo, vol. 1, p. 21.
16. Kuss J, Scheibner C, Gietl R. Carbonate platform to basin transition along an Upper Cretaceous to Lower Tertiary Syrian arc uplift. *Galala Plateaus Eastern Desert Egypt GeoArabia*. 2000;5:405–24. <https://doi.org/10.2113/geoarabia0503405>.
17. Abou El Saoud W. Geoenvironmental studies on New Cairo area and its vicinity, Egypt, using remote sensing data and geographic information systems. M. Sc. Thesis; 2006.
18. Höntzsch S, Scheibner C, Kuss JM, Marzouk AM, Rasser MW. Tectonically driven carbonate ramp evolution at the southern Tethyan shelf: the Lower Eocene succession of the Galala Mountains, Egypt. *Facies*. 2011;57(1):51–72. <https://doi.org/10.1007/s10347-010-0229-X>.
19. El-Desoky HM, El-shafey RE. The Oligo—Miocene Volcanism of the Red Sea Rift Valley: petrology and geochemistry of the volcanic activity in the Northwestern Sinai Egypt. *Nat Sci*. 2016. <https://doi.org/10.7537/marsnsj140816.22>.
20. Geologic map of Egypt 1: 2000000. Egyptian Geological Survey and Mining Authority. EGSM, Cairo; 1981.
21. El-Hadidy SM, Alshehri F, Sahour H, Abdelmalik KW. Detecting hydrocarbon micro-seepage and related contamination, probable prospect areas, deduced from a comparative analysis of multispectral and hyperspectral satellite images. *J King Saud Univ Sci*. 2022;34:6. <https://doi.org/10.1016/j.jksus.2022.102192>.
22. El-Hadidy SM. The relationship between urban heat islands and geological hazards in Mokattam plateau, Cairo, Egypt. *Egypt J Remote Sens Space Sci*. 2021;24:547–57. <https://doi.org/10.1016/j.ejrs.2021.02.004>.
23. Rowan LC, Mars JC. Lithologic mapping in the Mountain Pass, California area using Advanced Spaceborne Thermal Emission and Reflection Radiometer (ASTER) data. *Remote Sens Environ*. 2003;84:350–66. [https://doi.org/10.1016/S0034-4257\(02\)00127-X](https://doi.org/10.1016/S0034-4257(02)00127-X).
24. Hewson RD, Cudahy TJ, Huntington JF. Geologic and alteration mapping at Mt Fitton, South Australia, using ASTER satellite-borne data. *Geosci Remote Sens Symp*. 2001;2:724–6. <https://doi.org/10.1109/IGARSS.2001.976615>.
25. Kalinowski A, Oiver S. ASTER mineral index processing manual, remote sensing applications geoscience Australia; 2004.
26. Volesky JC, Stern RJ, Johnson PR. Geological control of massive sulfide mineralization in the Neoproterozoic Wadi Bidah shear zone, southwestern Saudi Arabia, inferences from orbital remote sensing and field studies. *Precambrian Res*. 2003;123(2):235–47. [https://doi.org/10.1016/S0301-9268\(03\)00070-6](https://doi.org/10.1016/S0301-9268(03)00070-6).
27. Galehouse JS. Sedimentation analysis. New York: Wiley Interscience; 1971.
28. Picard DM. Classification of fine-grained sedimentary rocks. *J Sediment Res*. 1971. <https://doi.org/10.1306/74D7221B-2B21-11D7-8648000102C1865D>.
29. Carver RE. Heavy mineral separation. New York: Wiley; 1971.
30. Frondel C. Systematic mineralogy of uranium and thorium. *U.S. Geol Surv Bull*. 1958. <https://doi.org/10.3133/b1064>.
31. Heinrich EW. Economic geology of the rare earth elements. *Miner Mag*. 1958;98:265–73. <https://doi.org/10.1515/9781501509032-014>.
32. Dawood YH, Abd El-Naby HH. Mineralogy and genesis of secondary uranium deposits, Um Ara area, South Eastern desert, Egypt. *J Afr Earth Sci*. 2001;32(2):1–6. [https://doi.org/10.1016/S0899-5362\(01\)90009-0](https://doi.org/10.1016/S0899-5362(01)90009-0).
33. Dawood YH, Harbi HM, Abd El-Naby HH. Genesis of kasolite associated with aplite-pegmatite at Jabal Sayid, Hijaz region. *Kingdom Saudi Arab J Asian Earth Sci*. 2010;37:1–9. <https://doi.org/10.1016/j.jseaes.2009.05.007>.
34. Abd El-Naby HH, Dawood YH. Testing the validity of detrital zircon chemistry as a provenance indicator. *Arab J Geosci*. 2014;1:341–53. <https://doi.org/10.1007/s12517-012-0800-6>.
35. Garzanti E, Ando S, Francelanord C, Censi P, Vignola P, Galy V, Lupker M. Mineralogical and chemical variability of fluvial sediments 2 Suspended-load silt (Ganga-Brahmaputra, Bangladesh). *Earth Planet Sci Lett*. 2011;302:107–20. <https://doi.org/10.1016/j.epsl.2010.11.043>.
36. Wu KK, et al. Grain-size effect on rare earth elements in Pahang River and Kelantan River, Peninsular Malaysia: implications for sediment provenance in the southern South China Sea. *Cont Shelf Res*. 2019;189: 103977. <https://doi.org/10.1016/j.csr.2019.103977>.
37. Yang SY, Jung HS, Choi MS, Li CX. The Rare Earth Element compositions of the Changjiang (Yangtze) and Huanghe (Yellow) river sediments. *Earth Planet Sci*. 2002. [https://doi.org/10.1016/S0012-821X\(02\)00715-X](https://doi.org/10.1016/S0012-821X(02)00715-X).
38. Borst AM, et al. Adsorption of rare earth elements in regolith-hosted clay deposits. *Nat Commun*. 2020;11:4386. <https://doi.org/10.1038/s41467-020-17801-5>.
39. Hamza MF, El Aassy IE, Ahmed FY, Abdel-Rahman AA, Atta AM. Separation of uranium and rare earth elements with high purity from low-grade gibbsite-bearing shale ore by different chelating resins. *J Dispers Sci Technol*. 2012;33(4):482–9. <https://doi.org/10.1080/01932691.2011.574895>.
40. Gamal H, Mohrez WA, Abdelkareem A, Mashaal H, Abde El-Aziz HM, Abd E-F. Leaching of rare earth elements from gibbsite-bearing shale of southwestern Sinai, Egypt using ammonium sulfate via ion exchange mechanism. *Egypt J Chem*. 2023. <https://doi.org/10.21608/ejchem.2023.198156.7691>.

41. Gouveia MA, et al. Behavior of REE and major elements during weathering of granitic. *Evora Port Chem Geol.* 1993;107:293–6. [https://doi.org/10.1016/0009-2541\(93\)90194-N](https://doi.org/10.1016/0009-2541(93)90194-N).
42. Mongelli G. REE and other trace elements in a granitic weathering profile from “Serre.” South Italy *Chem Geol.* 1993;103:17–25. [https://doi.org/10.1016/0009-2541\(93\)90288-T](https://doi.org/10.1016/0009-2541(93)90288-T).
43. Nesbitt HW. Mobility and fractionation of rare earth elements during weathering of a granodiorite. *Nature.* 1979;279(5710):206–10. <https://doi.org/10.1038/279206a0>.
44. Braun JJ, Viers J, Dupre B, Polve M, Ndam J, Muller JP. Solid/liquid REE fractionation in the lateritic system of Goyoum, East Cameroon: the implication for the present dynamics of the rocks covers of the humid tropical regions. *Geochim Cosmochim Acta.* 1998;62(2):273–99. [https://doi.org/10.1016/S0016-7037\(97\)00344-X](https://doi.org/10.1016/S0016-7037(97)00344-X).
45. McLennan SM. Rare earth elements in sedimentary rocks: influence of provenance and sedimentary processes. *Rev Miner Geochem.* 1989;21:169–200. <https://doi.org/10.1515/9781501509032-010>.
46. Migaszewski ZM, Gałuszka A. The characteristics, occurrence, and geochemical behavior of rare earth elements in the environment: a review. *Crit Rev Environ Sci Technol.* 2015;45(5):429–71. <https://doi.org/10.1080/10643389.2013.866622>.
47. Boesche NK, et al. Hyperspectral REE (rare earth element) mapping of outcrops—applications for neodymium detection. *RemoteSensin.* 2015;7:5160–86. <https://doi.org/10.3390/rs70505160>.

Publisher’s Note Springer Nature remains neutral with regard to jurisdictional claims in published maps and institutional affiliations.